Journal of Fluids and Structures (2002) **16**(6), 773–794
doi:10.1006/jfls.449. available online at http://www.idealibrary.com on IDEAL®

A NUMERICAL SIMULATION OF VORTEX SHEDDING FROM AN OSCILLATING CIRCULAR CYLINDER

E. Guilmineau and P. Queutey

Laboratoire de Mécanique des Fluides, CNRS UMR 6598 Ecole Centrale de Nantes B.P. 92101, 44321 Nantes Cedex 3, France

(Received 4 December 1999; accepted in final form 12 November 2001)

Vortex shedding from an oscillating circular cylinder is studied by numerical solutions of the two-dimensional unsteady Navier–Stokes equations. A physically consistent method is used for the reconstruction of velocity fluxes which arise from discrete equations for the mass and momentum balances. This method ensures a second-order accuracy. Two phenomena are investigated and, in both cases, the cylinder oscillation is forced. The first is the flow induced by the harmonic in-line oscillation of cylinder in water at rest. The Reynolds number is equal to 100 and the Keulegan–Carpenter number is equal to 5. A comparison of phase-averaged velocity vectors between measurements and predictions is presented. Applying the widely used model of Morison to the computed in-line force history, the drag and the inertia coefficients are calculated and compared for different grid levels. Using these to reproduce the force functions, deviations from those originally computed are revealed. The second problem is an investigation of a transversely oscillating cylinder in a uniform flow at fixed Reynolds number equal to 185. The cylinder oscillation frequency ranges between 0·80 and 1·20 of the natural vortex-shedding frequency, and the oscillation amplitude is 20% of the cylinder diameter. As the frequency of excitation of the cylinder increases relative to the inherent vortex formation frequency, the initially formed concentration of vorticity moves closer to the cylinder until a limiting position is reached. At this point, the vorticity concentration abruptly switches to the opposite side of the cylinder. This process induces distinct changes of the topology of the corresponding streamline patterns.

1. INTRODUCTION

The computation of the fluid forces on an offshore structure is one of the primary tasks in the design of the structures. It is also one of the most difficult tasks since it involves the complexity of the interaction of waves with the structure. Therefore, to study this phenomenon, the problem of a cylindrical body oscillating in the fluid has received a great deal of attention. The problem of a cylinder oscillating laterally (cross-flow) in a free stream is well known and has been documented by many investigators, a few of whom are Bishop & Hassan (1964), the first researchers to investigate the effect of body oscillation on vortex shedding, Koopmann (1967), Griffin (1971), Bearman & Currie (1979), Sarpkaya (1979), Bearman (1984) and Öngoren & Rockwell (1988). An oscillating cylinder in a quiescent fluid, or the converse situation of oscillating flow past a stationary cylinder, is also an effective representation of wave–cylinder interaction in the area of ocean engineering. Comprehensive experimental results and reviews of oscillating flow may be found in Sarpakaya & Isaacson (1981), Bearman *et al.* (1985), Williamson (1985) and Obasaju *et al.* (1988).

0889-9746/02/060773 + 22 $35.00/0

In the case of a cylinder oscillating transversely in a free-stream, the relevant parameters, besides the Reynolds number $\mathrm{Re} = U_\infty D/\nu$ where U_∞ is the free-stream velocity, D the cylinder diameter and ν the kinematic viscosity of fluid, are the oscillating amplitude, A_e, and the excitation frequency, f_e. In the present study, the translation motion $x_2(t)$ is given by the harmonic oscillation $x_2(t) = A_e \cos(2\pi f_e t)$.

Bishop & Hassan (1964) found the jump in the phase angle, ϕ, between the transverse force and body motion displacement that occurs when the frequency of oscillation is varied around the natural shedding frequency, f_o, which is called the synchronization condition. These variations in phase angle are associated with the change in sign of the energy transfer between the fluid and the cylinder. Koopmann (1967) also investigated the effect of forced transverse oscillation of a cylinder on vortex shedding. His main concern was to determine the synchronization condition, or lock-in boundaries. He found that the lock-in occurred only above a threshold amplitude of oscillation and that the lock-in range increased with increasing amplitude.

The work of Zdravkovich (1982) and Öngoren & Rockwell (1988) showed that the phase jump can be explained by a change of the timing of the vortices being shed. They noticed, for frequencies of oscillation above the natural shedding frequency, a vortex formed on one side of the cylinder and was shed when the cylinder was near the maximum amplitude on the opposite side. On decreasing the frequency of oscillation, the timing changes suddenly, such that a vortex is shed when the cylinder is at its maximum amplitude on the same side. In a recent numerical investigation, Blackburn & Henderson (1999) suggest that the dynamics of the change in phase of shedding arise from a conception between two different mechanisms of vorticity.

In all previous studies, the amplitude of oscillation is small. Williamson & Roshko (1988), experimentally, and Meneghini & Bearman (1995), numerically, present two attempts to this work to large amplitudes of oscillation. They found a series of synchronization regions, which they classified in terms of the number of vortices shed per cycle of oscillation.

A periodic oscillating flow over a circular cylinder in a fluid at rest is characterized by the Reynolds number, $\mathrm{Re} = U_m D/\nu$, where U_m is the maximum oscillatory velocity, and the Keulegan–Carpenter number, $\mathrm{KC} = U_m/f_e D$ where f_e is the frequency of the oscillatory flow. A third often-used parameter, β, is a frequency parameter which is equal to Re/KC. In the present study, the translation motion $x_1(t)$ is given by the harmonic oscillation $x_1(t) = -A_e \sin(2\pi f_e t)$, where A_e is the amplitude of the oscillatory flow. Thus, the Keulegan–Carpenter number can be written as $\mathrm{KC} = 2\pi A_e/D$.

When $\mathrm{KC} \ll 1$, the flow past an oscillating cylinder remains attached and symmetrical. Honji (1981) observed that the flow was unstable and became three-dimensional at small KC. Sarpkaya (1986) investigated in detail the influence of KC and β on the occurrence of the Honji instability and found that, as β increased, the vortex structure appeared at lower values of KC. Experimental investigations of the oscillatory flow around a circular cylinder at small KC show that the flow can be classified into a number of different flow regimes governed mainly by KC and with a weak dependency on Re. At KC values below about 1 or 2, depending on β, the flow is symmetrical and is thought to remain attached. In the next regime, up to approximately $\mathrm{KC} = 4$, the flow separates but remains symmetrical. Between $\mathrm{KC} = 4$ and 7, the asymmetric shedding of a pair of opposite sign vortices is observed in each half cycle. At KC values between 7 and 15, the majority of the vortex-shedding activity takes place on only one side of the cylinder. The shed vortices are convected away to one side of the cylinder, roughly normal to the main flow direction, and the flow regime is termed a transverse vortex street. For KC between 15 and 24, the flow enters the diagonal shedding mode. For KC between 24 and 32, three full vortices are

formed during each half cycle, and the vortex pairs are convected away from the cylinder during a complete cycle. This type of flow activity continues as KC increases with more and more vortex pairs being formed and shed per flow cycle.

Several numerical solutions of the unsteady two-dimensional Navier–Stokes equations for flow around a circular cylinder at low KC values and relatively low β parameter have been reported in the literature: Stansby & Smith (1991), Justesen (1991), Lin *et al.* (1996), Sun & Dalton (1996) and Dütsch *et al.* (1998).

The objective of the present study is to examine computationally the vortex shedding from an oscillating circular cylinder in two configurations: cross-flow oscillations with a free-stream and in-line oscillations in a fluid at rest. For both cases, a comparison with experimental data is carried out.

2. GOVERNING EQUATIONS

The aim is a computational study to predict the two-dimensional fluid motion induced by the oscillation of a circular cylinder. Considering the cylinder motion in a fluid, two reference frames can be used. One, the inertial system, $\boldsymbol{x}_a$, is connected to the stationary fluid channel. The other moves with the cylinder and is therefore an accelerated reference system with its Cartesian coordinates denoted $\boldsymbol{x}_k$. The second approach is used. Both are connected by the relationship,

$$\boldsymbol{x}_a = \boldsymbol{x} + \boldsymbol{x}_e, \tag{1}$$

where $\boldsymbol{x}_e$ is the position of the accelerating reference system. Differentiating equation (1) in time, the velocity $\boldsymbol{U}_a$ of a fluid element in the inertial system can be written as

$$\boldsymbol{U}_a = \boldsymbol{U} + \boldsymbol{U}_e, \tag{2}$$

where $\boldsymbol{U}$ is the mean Cartesian velocity in the accelerated system and $\boldsymbol{U}_e$ is the corresponding system velocity, i.e., the cylinder velocity.

Equations are presented throughout in nondimensional form. The velocity scale is the reference velocity, U_{ref} ($U_{\text{ref}} = U_\infty$ for cross-flow oscillations and $U_{\text{ref}} = U_m$ for in-line oscillations), the length scale is the cylinder diameter, D, and time is nondimensionalized by the aerodynamic scale D/U_{ref}.

The unsteady incompressible Navier–Stokes equations can be written in the following strong-conservation form:

$$\nabla \cdot \boldsymbol{U} = 0, \tag{3}$$

$$\frac{\partial \boldsymbol{U}}{\partial t} + \nabla \cdot \boldsymbol{F} = \frac{\partial \boldsymbol{U}_e}{\partial t}, \tag{4}$$

with the Cartesian components, F_{kj}, of the momentum flux $\boldsymbol{F}_k$, given by

$$F_{kj} = U_k\, U_j + \delta_{jk} P - \frac{1}{\text{Re}} \frac{\partial U_k}{\partial x_j}. \tag{5}$$

Here, P is the pressure, $\text{Re} = U_{\text{ref}} D/\nu$ is the Reynolds number, and δ_{ij} is the Kronecker symbol.

For the applications to be considered, the complexity of the geometry prevents the use of Cartesian coordinates. Numerical coordinate transformations are required in order to facilitate the application of boundary conditions and transform the physical domain in which the flow is studied into a rectangular domain $\{\xi^1, \xi^2\}$. This computational domain consists of a set of unique squares of sides $\Delta\xi^i = 1$, $i = 1, 2$.

This partial transformation of equations (3)–(5) yields the following equations:

$$\frac{1}{J}\frac{\partial b_j^i U_j}{\partial \xi^i} = 0, \tag{6}$$

$$\frac{\partial U_k}{\partial t} + \frac{1}{J}\frac{\partial b_j^i F_{kj}}{\partial \xi^i} = \frac{\partial U_{ek}}{\partial t}, \tag{7}$$

with

$$F_{kj} = U_k U_j + P\delta_{jk} - \frac{a_j^m \partial U_k}{\mathrm{Re}\partial \xi^m}, \tag{8}$$

where the Jacobian J of the transformation from the computational space of the coordinates $\{\xi^i\}$ to the physical space of the Cartesian coordinates $\{x_i\}$ can be expressed by $J\delta_i^j = \boldsymbol{a}_i \cdot \boldsymbol{b}_i$. The area vector $\boldsymbol{b}$ is given by $\boldsymbol{b} = \boldsymbol{a}_j \times \boldsymbol{a}_k$ (i, j, k in cyclic order) and the modulus of the covariant vector $\boldsymbol{a}_i$ by $\boldsymbol{a}_i = \partial \boldsymbol{R}/\partial \xi^i$, where $\boldsymbol{R}$ is the position vector.

The boundary condition on the cylinder surface is the no-slip condition,

$$U_1 = 0, \quad U_2 = 0, \tag{9}$$

and at the outer boundary, the velocity $\boldsymbol{U}$ oscillates with the negative cylinder velocity,

$$\boldsymbol{U} = \boldsymbol{U}_a - \boldsymbol{U}_e, \tag{10}$$

where $\boldsymbol{U}_a$ is the velocity in the inertial system at the outer flow boundary.

3. NUMERICAL APPROACH

3.1. Discrete Equations

The collocated cell-centred grid layout is used. So, the Cartesian velocity components and the pressure share the same location at the centre of the control volume (Figure 1).

In the following, $U_k(\mathrm{NN})$ will be the unknown kth Cartesian velocity component at point NN and the flux at cell interface pN is identified as $(JU^i)(\mathrm{pN})$. The discrete divergence of the flux ϕ over the control volume is simply

$$(\Delta_i \phi^i)(\mathrm{NN}) = \phi^1(\mathrm{pN}) - \phi^1(\mathrm{mN}) + \phi^2(\mathrm{Np}) - \phi^2(\mathrm{Nm}), \tag{11}$$

so that the discrete continuity equation results from $\phi = \boldsymbol{b}^i \cdot \boldsymbol{U}$.

The time derivative is discretized using a second-order-accurate fully implicit backward Euler method involving the time levels $t^0 = t - \Delta t$ and $t^{00} = t - 2\Delta t$ besides the actual time level t. We then have

$$\begin{aligned} &\frac{\partial \phi}{\partial t} \approx e_1\Phi + e_0\Phi^0 + e_{00}\Phi^{00}, \\ &e_1 = \frac{3}{2\Delta t}, \quad e_0 = -\frac{2}{\Delta t}, \quad e_{00} = \frac{1}{2\Delta t}, \\ &\Phi = \phi(t), \quad \Phi^0 = \phi(t^0), \quad \Phi^{00} = \phi(t^{00}). \end{aligned} \tag{12}$$

Using equations (11) and (12) yields the following motion equations:

$$\frac{1}{J(\mathrm{NN})}\Delta_i(b_j^i U_j)(\mathrm{NN}) = 0, \tag{13}$$

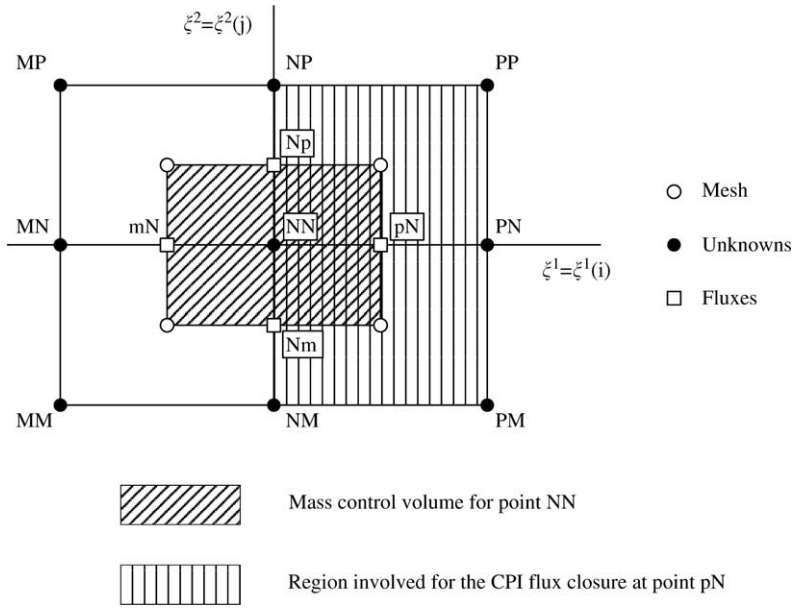

Figure 1. Schematic sketch of presently used notation and influence stencil of point NN for CPI method.

$$e_1\, U_k(\mathrm{NN}) + e_0\, U_k^0(\mathrm{NN}) + e_{00}\, U_k^{00}(\mathrm{NN}) + \frac{1}{J(\mathrm{NN})}\Delta_i(b_j^i\, F_{kj})(\mathrm{NN}) = \frac{\partial U_{ek}(\mathrm{NN})}{\partial t}. \tag{14}$$

In the discrete divergence at point NN in equation (14), the linearized momentum flux $\boldsymbol{b}^i\, \boldsymbol{F}_k$ is defined at interfaces pN, mN, Np and Nm as indicated in equation (11). For instance, we have

$$\boldsymbol{b}^i\, \boldsymbol{F}_k(\mathrm{pN}) = \left[(\boldsymbol{b}^i \cdot \boldsymbol{U}^*)U_k + P\, b_k^i - \frac{\boldsymbol{b}^i \cdot \boldsymbol{a}^m}{\mathrm{Re}}\frac{\partial U_k}{\partial \xi^m}\right](\mathrm{pN}), \tag{15}$$

where $\boldsymbol{U}^*$ is a prediction of the velocity field at the actual time. An iterative procedure is thus required at time t in order to update $\boldsymbol{U}^*$, starting with $\boldsymbol{U}^* = \boldsymbol{U}^0$.

The last term of equation (14) is not discretized by equation (12). The motion of the cylinder is known analytically, thus we can determine the velocity of the cylinder and its acceleration analytically.

3.2. The Reconstruction Problem

After integrating fluxes over the control volume, it appears that besides unknown nodal values of the Cartesian velocity components, expressions such as equation (15) involve the values $U_k(pN)$ which are also unknown, but at points which are not nodal points. These Cartesian velocity components are denoted $U_k(f)$ where f is pN, mN, Np or Nm. This introduces the so-called reconstruction problem: fluxes such as U_k(pN) which are not defined at nodal points must be expressed in terms of nodal unknowns. The interpolation procedure, which solves the reconstruction problem, must avoid spurious pressure modes which may exist when collocated grids are used. One of the most efficient ways to

overcome this difficulty is to use a physical interpolation approach in which a velocity value such as U_k(pN) is expressed not only in terms of values of U_k at the neighbouring nodes of pN, the set of which (Figure 1) is denoted NB(pN) = {NN, PN, PM, PP, NP, NM}, but also in terms of values of other velocity components and pressure at NB(pN). The most classical approach in this respect is the Rhie & Chow (1983) interpolation. Its drawbacks, as well as those of another interpolation practice due to Schneider & Raw (1987), have been analysed by Deng *et al.* (1994a,b), where the so-called consistent physical interpolation (CPI) method is proposed. The application of the CPI to unsteady laminar flows has been further developed by Deng *et al.* (1994a) for airfoil problems and extended to turbulent flow by Guilmineau *et al.* (1997a).

The CPI method determines U_k(pN) from the solution of the convective form of the momentum equations at point pN. This interpolation involves the set of neighbours NB(pN) of influencing node (Figure 2). For other interfaces of the control volume, the sets of active neighbours are

$$NB(\mathrm{mN}) = \{\mathrm{MN, NN, MP, NP, MM, MN}\},$$

$$NB(\mathrm{Np}) = \{\mathrm{NN, NP, NM, PM, PN, PP}\},$$

$$NB(\mathrm{Nm}) = \{\mathrm{NN, PN, MN, PM, NM, MM}\}.$$

Upon substitution of closures written at pN, mN, Np and Nm into the discrete momentum equation (14), where relations such as equation (15) have been accounted for,

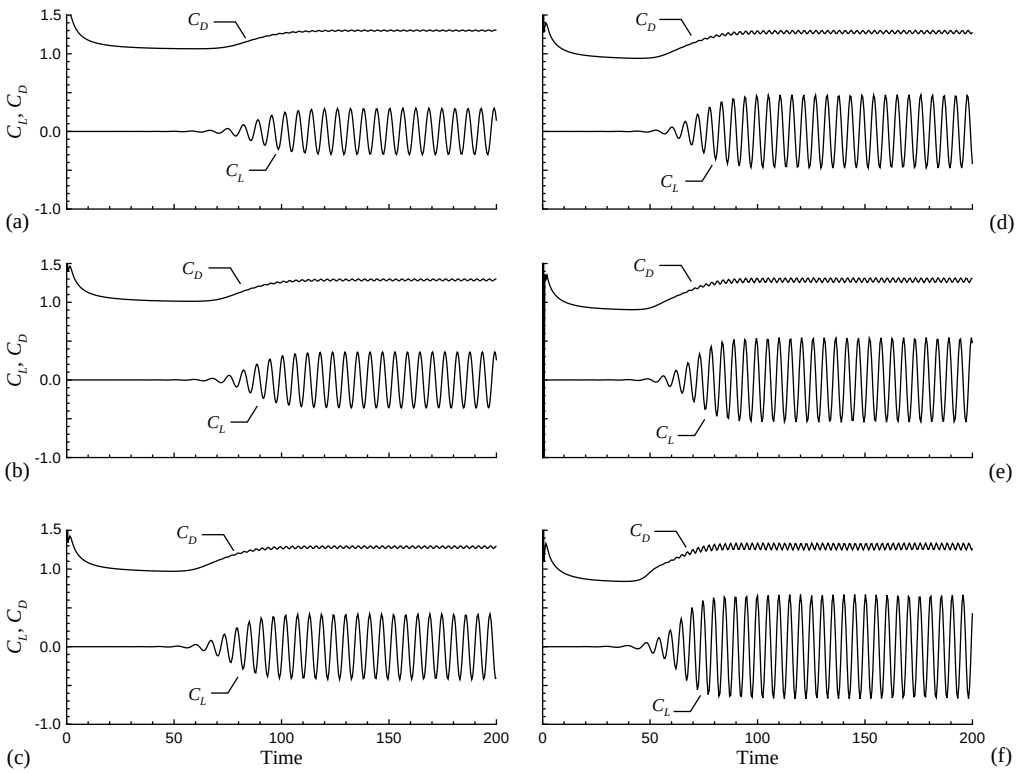

Figure 2. Drag and lift coefficients for a nonoscillating cylinder at different Reynolds numbers: (a) Re = 95; (b) Re = 110; (c) Re = 126; (d) Re = 140; (e) Re = 160; (f) Re = 200.

we obtain the discrete scheme for the momentum equations where the velocity and pressure unknowns are located only at NN and at the eight nodal neighbours of the set $NB(\mathrm{NN}) = \{\mathrm{MM}, \mathrm{MN}, \mathrm{MP}, \mathrm{NM}, \mathrm{NP}, \mathrm{PM}, \mathrm{PN}, \mathrm{PP}\}$. The substitution of the same closures into equation (13) yields a discrete scheme for a nine-point pressure equation. Its ensures a second-order accuracy and numerical stability Deng *et al*. (1994b). Another important feature of the CPI scheme is that it ensures both mass and momentum conservation over the same control volume.

3.3. Pressure–Velocity Coupling Algorithm

The algorithm which yields a coupled solution of the momentum equation and the continuity equation is directly inspired by the Pressure Implicit with Splitting of Operators (PISO) algorithm Issa (1985): (a) initialize the velocity field and the pressure field at $t = t^0$; (b) new time step $t = t + \Delta t$; (c) start iterative procedure with $U_k = U_k^0$, $P = P^0$, $U_k(f) = U_k^0(f)$; (d) compute the reconstruction coefficients from the field of step (c); (e) solve the momentum equations to obtain a new prediction for U_k; (f) solve the continuity equation to obtain pressure P with coefficients obtained from step (d) and U_k from step (e); (g) correct the velocity field with coefficients from step (d), U_k from step (d) and P from step (f); (h) reconstruction at interfaces to get $U_k(f)$ with coefficients from step (d), P from step (f) and U_k from step (g); (i) if the nonlinear residuals are low enough, go to step (a) and update t; otherwise, go to step (c) and update the iteration count within the time step.

4. RESULTS

4.1. Preamble

Before presenting results, some numerical parameters need to be specified. The equations are solved on an O-type structured grid. A mesh with 120 points in the angular direction and 100 points in the radial direction is used. The first points of the mesh in the fluid are located at $y = 0{\cdot}001D$ away from the wall and the outer flow boundary is located at 25 diameter lengths away from the cylinder. A nondimensional time step, $U_\infty \Delta t/D$, equal to 0·002 is used.

For each time step, a reduction of nonlinear residuals for the discrete momentum equations is required. By default, we use 20 nonlinear iterations at each time step, so that a reduction by 2·0–2·5 orders of the magnitude of the residuals of the discrete momentum equations is required. Also, the divergence of the velocity field is decreased to between 10^{-6} and 10^{-9}. These parameters were already used to compute the deep dynamic stall of a pitching NACA 0012 airfoil Guilmineau *et al* (1997*b*) and the deep dynamic stall on several airfoil sections Guilmineau *et al*. (1999).

4.2. Fixed Cylinder

While not the main focus of this study, the simulation of the two-dimensional flow past a fixed cylinder at different Reynolds numbers ($85 < \mathrm{Re} < 200$) is included here as a basis of comparison with other numerical and experimental results for a complete validation of the code.

Figure 2 shows the time histories of the lift and drag coefficients for different Reynolds numbers. It can be seen that the lift force settles to a regular sinusoidal function after the onset of wake instability leads to vortex shedding. The lift and drag amplitudes increase as

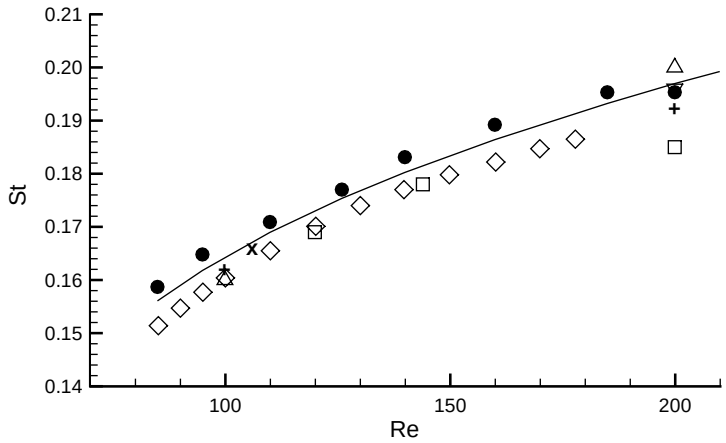

Figure 3. Strouhal number versus Reynolds number for a nonoscillating cylinder: ●, present simulations; □, Griffin (1971), experimental; ◇, Williamson (1989), experimental; △, Braza *et al.* (1986), numerical; ▽, Meneghini & Bearman (1995), numerical; ×, Anagnostopoulos (1997), +, Zhou *et al.* 1999, numerical; ——, Williamson (1998), universal strouhal curve.

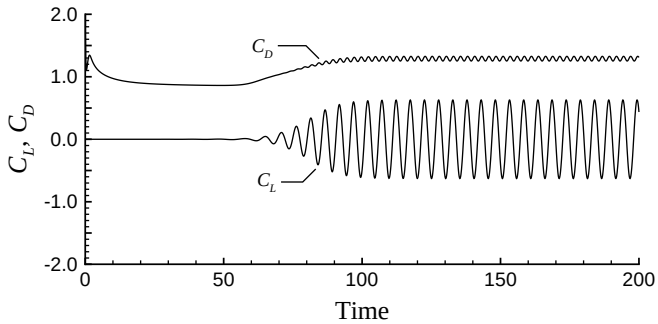

Figure 4. Lift and drag coefficients for a nonoscillating cylinder at Re = 185.

TABLE 1

Numerical and experimental values of St, $\bar{C}_D$ and $C_{L\,\mathrm{r.m.s.}}$ at Re = 185 (fixed cylinder)

	$\bar{C}_D$	$C_{L\,\mathrm{r.m.s.}}$	St
Mesh = 120 × 100, $Dt = 0{\cdot}002$	1·287	0·443	0·195
Experimental results	1·28	—	0·19
Numerical results Lu & Dalton (1996)	1·31	0·422	0·195
"Universal" Strouhal Williamson (1988)			0·193

the Reynolds number increases. Figure 3 presents the Strouhal–Reynolds curve. We also compare with numerical and experimental results and with the "universal" Strouhal–Reynolds number relation given by Williamson (1988). The agreement is quite good.

For the cross-flow oscillations, the Reynolds number is Re = 185. Let us look in more detail at the flow past a fixed cylinder for this Reynolds number. Figure 4 presents the drag and lift for this case. The average drag coefficient, $\bar{C}_D$, the r.m.s value of the lift coefficient, $C_{L\,\mathrm{r.m.s.}}$, and the Strouhal number, St, are reported in Table 1. They are compared with

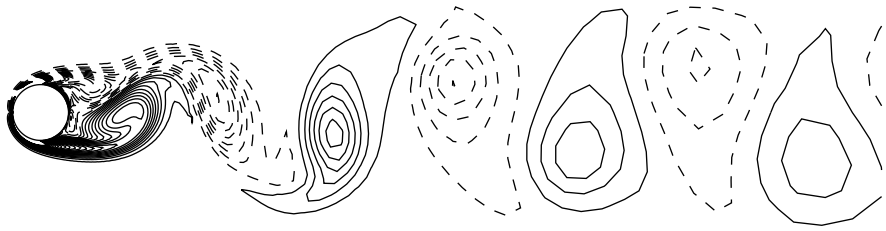

Figure 5. Wake vorticity contours for a nonoscillating cylinder at Re = 185. (—— : positive values; - - - - : negative values).

values reported in Lu & Dalton (1996). The Strouhal number is also compared with the values based on a relation given by Williamson (1988). The agreement is good. Figure 5 shows the vortex pattern in the wake.

4.3. In-Line Oscillations

The parameter set of the present investigation is Re = 100 and KC = 5, according to experimental and numerical results of Dütsch *et al.* (1998).

The computed flow is characterized by stable, symmetric and periodic vortex shedding. Two fixed stagnation points at the front and back of the cylinder exist. The resulting vortex dynamics can be described as follows. As the oscillating cylinder moves in the forward direction, at the front of the cylinder an upper and lower boundary layer develops, which separates at the same upper and lower position on the cylinder wall. The separating flow creates two counter-rotating vortices of the same magnitude of strength, resulting in the same vortex shape. This creation of vorticity is coming to an end when the maximum front location of the cylinder is reached and the cylinder starts its backward motion, creating the same vortex formation on the other side of the cylinder, i.e., in the new wake of the cylinder flow. In addition, the backward motion of the cylinder causes a splitting of the vortex pair, which is produced by the forward motion, and finally wake reversal occurs. A sequence of these periodic flow patterns caused by the forward and backward motion is shown in Figure 6.

The good agreement between the experimental Dütsch *et al.* (1998) and numerical results is indicated by the comparisons provided in Figure 7 of measured and predicted velocity fields for three phase angles ($= 2\pi f_e t$) of the cylinder motion.

To compare further the experimental Dutsch *et al.* (1998) and numerical results, the data are processed to yield local phase-averaged velocity information. Data are provided in Figure 8 for three phase angles of the oscillatory cylinder motion, showing velocity profiles at four locations for a constant x_1-position. The comparison is considered to be very satisfactory and equivalent to the numerical results of Dütsch *et al.* (1998).

The numerical predictions are analysed with respect to the independence of the spatial grid sizes and the computational time step. The in-line force, $F_X(t)$, acting on the cylinder can be computed and the resulting information is employed to calculate the drag coefficient, C_D, and the added-mass coefficient, C_I, of the Morison equation (Chakrabarti 1987). These coefficients are evaluated by Fourier analysis. By evaluating the numerical results for various grid sizes the in-line force is computed yielding the results presented in Table 2. With the 120×100 mesh, we have a difference of 1% for the drag coefficient compared to the value obtained with the finest grid and a difference of 0·07% for the added-mass coefficient. The C_D and C_I values are $C_D = 2{\cdot}080$ and $C_I = 1{\cdot}434$. Dutsch *et al.* (1998) found numerically, using a velocity–pressure formulation, $C_D = 2{\cdot}09$ and

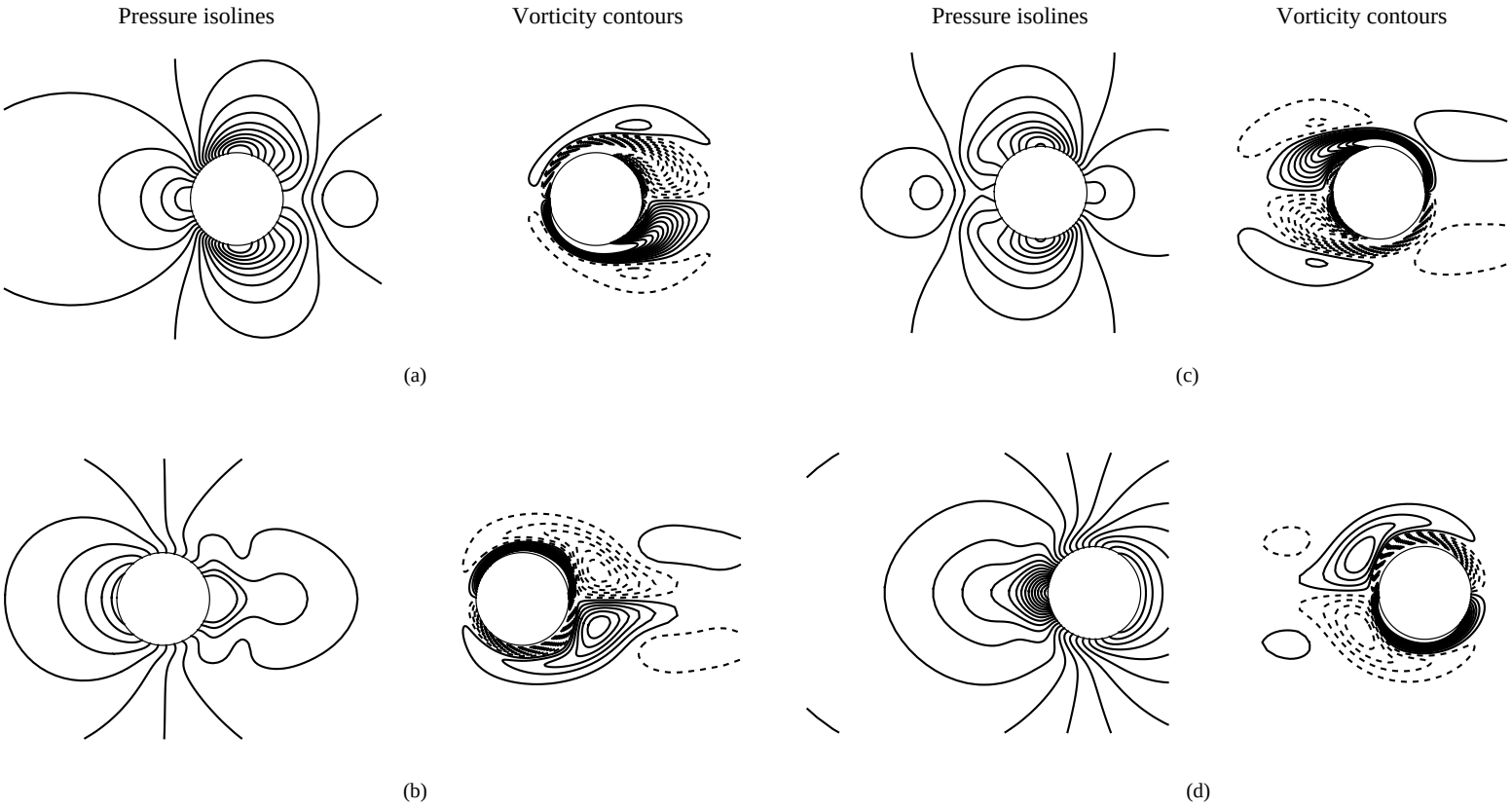

Figure 6. Pressure and vorticity isolines for Re = 100 and KC = 5 at different phase positions (phase position = $2\pi f_e t$). (a) 0°; (b) 95° (c) 193° and (d) 288°.

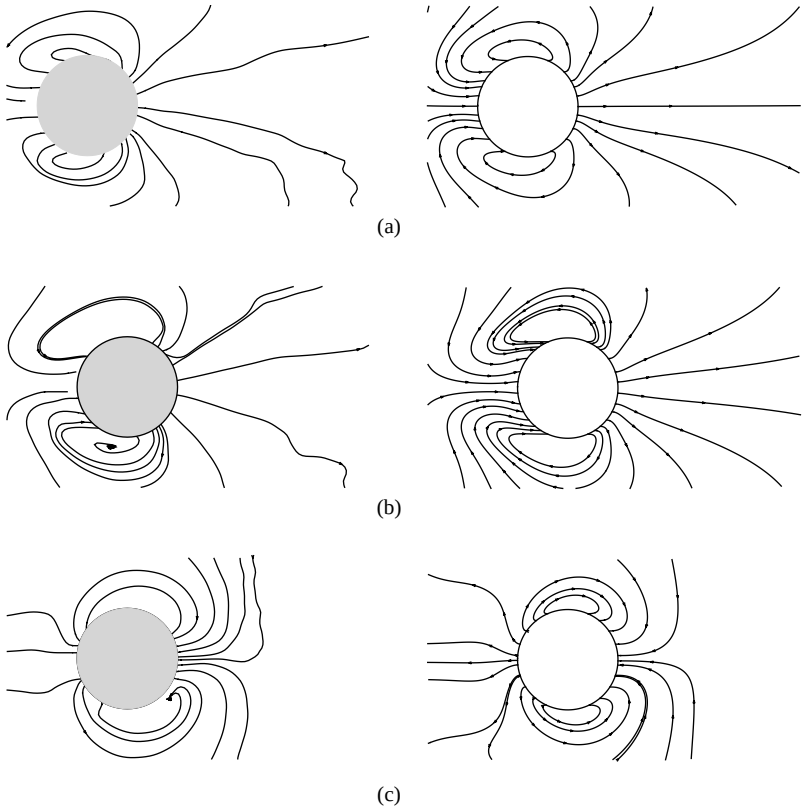

Figure 7. Measured Dutsch *et al.* (1998) (left) and computed streamlines (right) in the vicinity of the cylinder at Re = 100 and KC = 5 at different phase positions (phase position = $2\pi f_e t$): (a) 180°; (b) 210°; (c) 330°.

$C_I = 1{\cdot}45$ for a mesh with 384 points in the angular direction and 256 points in the radial direction, and a time step $\Delta t/T_e = 1/720$, where T_e is the period of the oscillatory flow, $T_e = 1/f_e$.

In Figure 9, the dimensionless total force variation with time is presented according to the parameters of the numerical predictions of Table 2. The computed results are compared with the $F_X(t)$-time variation prediction according to the Morison equation. This figure reveals that the numerical predictions are in phase with very little difference in peak as noted by Lu *et al.* (1997). Using the Morison equation, we do not correctly predict the extremes of the in-line force. This remark is in keeping with the numerical results of Dütsch *et al.* (1998), which, for each time step and each variable, the residual had to decrease at least of five orders of magnitude. Consequently, the discordance between the Morison equation and present simulations is not due to a grid not fine enough and a convergence not sufficient.

This study has allowed to determine a minimum grid size to obtain acceptable results. Thus, we choose the mesh of 120×100 for use in the next section of the paper.

4.4. Cross-Flow Oscillations

We have performed calculations for Re = 185, $A_e/D = 0{\cdot}2$ and $0{\cdot}8 \leqslant f_e/f_o \leqslant 1{\cdot}2$, where f_o is the natural shedding frequency from the stationary cylinder. These calculations are

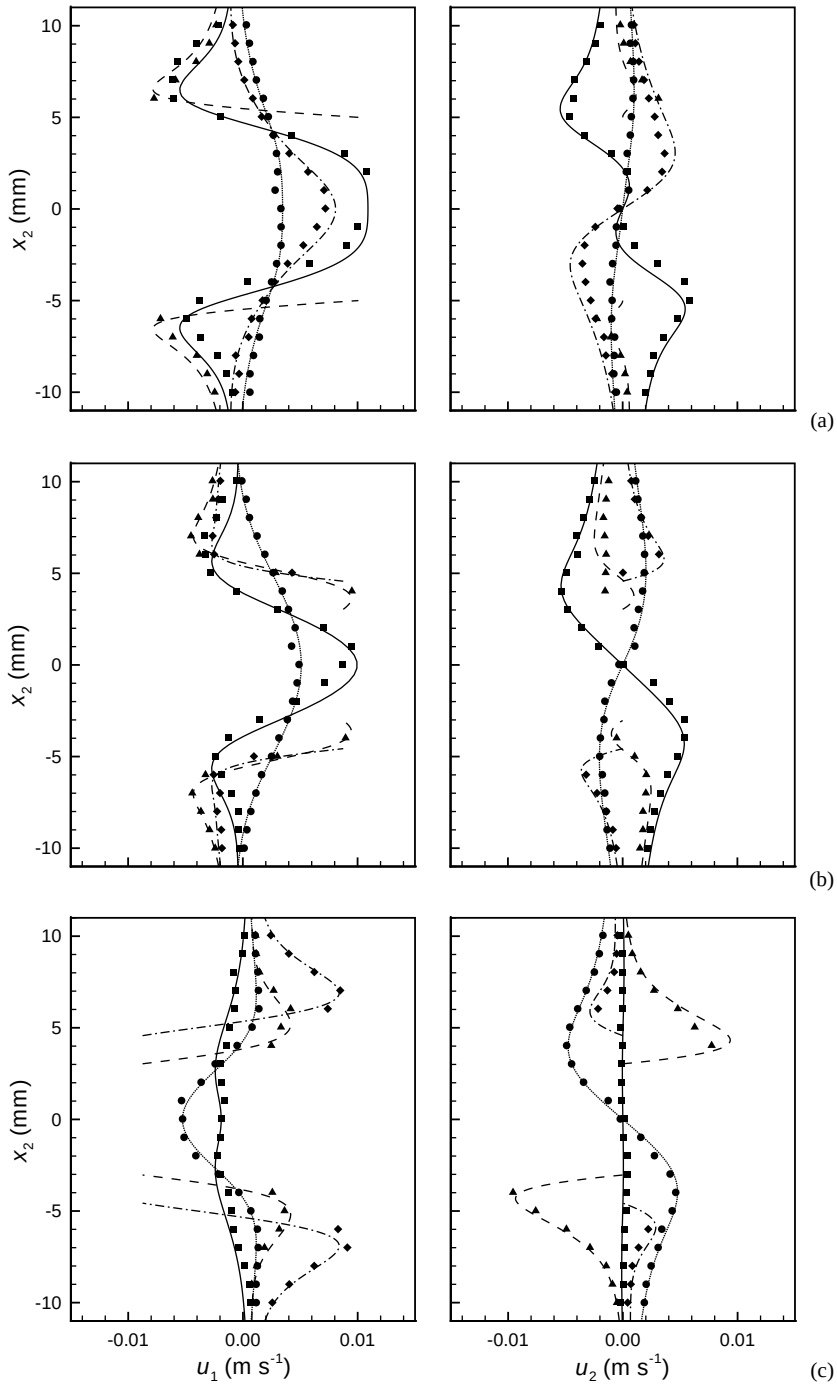

Figure 8. Comparison of the velocity components for Re = 100 and KC = 5 between present computation and experimental investigation Dütsch *et al.* (1998) at different phase positions (phase position = $2\pi f_e t$); (a) 180°; (b) 210°; (c) 330°; —, ■, computation and experiments, $x = -6$ mm; - - - -, ▲, computation and experiments, $x = 0$ mm; – – – –, ◆, computation and experiments, $x = 6$ mm; ....., ●, computation and experiments, $x = 12$ mm.

TABLE 2

Drag and added-mass coefficients for Re = 100 and KC = 5. Comparison of different grid resolutions

Mesh	C_D	C_I
120 × 100	2·059	1·433
120 × 200	2·063	1·429
180 × 100	2·069	1·440
180 × 200	2·072	1·436
240 × 100	2·074	1·445
240 × 200	2·078	1·441
360 × 300	2·081	1·436
480 × 400	2·080	1·434
Dutsch *et al.* (1998)	2·090	1·450

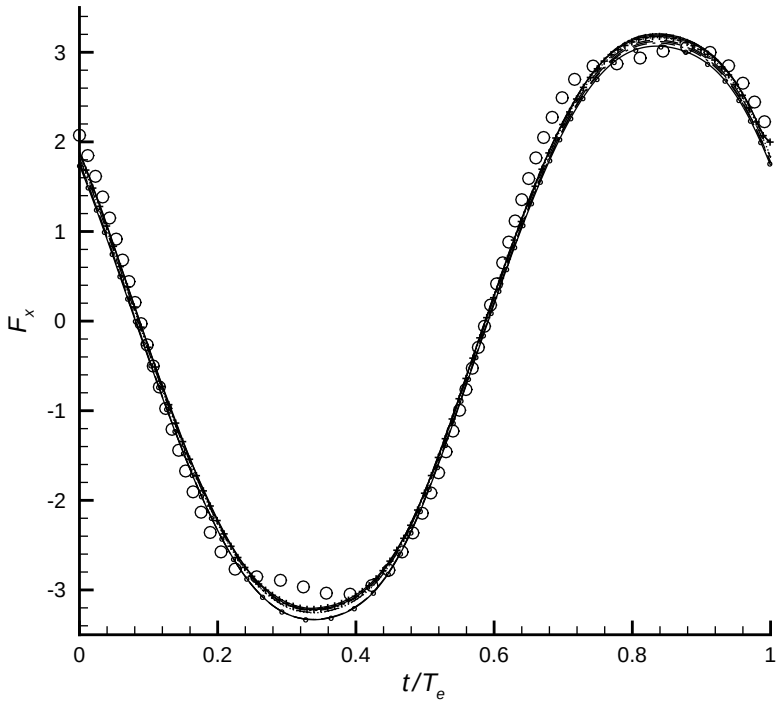

Figure 9. In-line force computed on different grid levels for Re = 100 and KC = 5: ——◦——, mesh = 120×100 – – – – –, mesh = 120×200; – - – - –, mesh = 180×100; ....., mesh = 180×200; — — — —, mesh = 240×100; – - - - – - –, mesh = 240×200; ———, mesh = 360×300; —— + ——, mesh = 480×400; ○, Morison equation.

two-dimensional based on the observations of Gu *et al.* (1994) that the near-wake structure is due to the forced oscillations at Reynolds number 185. Our goal is to reproduce experimental results of Gu *et al.* (1994). With numerical simulations of forced oscillations, we want to study the phenomenon of vortex switching.

Figure 10 shows the drag and lift coefficients, in the inertial reference frame, over the range of values of f_e/f_o considered. We can note that drag and lift behaviours are fairly regular once vortex shedding is established. For values of f_e/f_o greater than 1·0, both the drag and lift exhibit regular signs of the influence of a higher harmonic. As the excitation frequency increases, the beating frequency decreases.

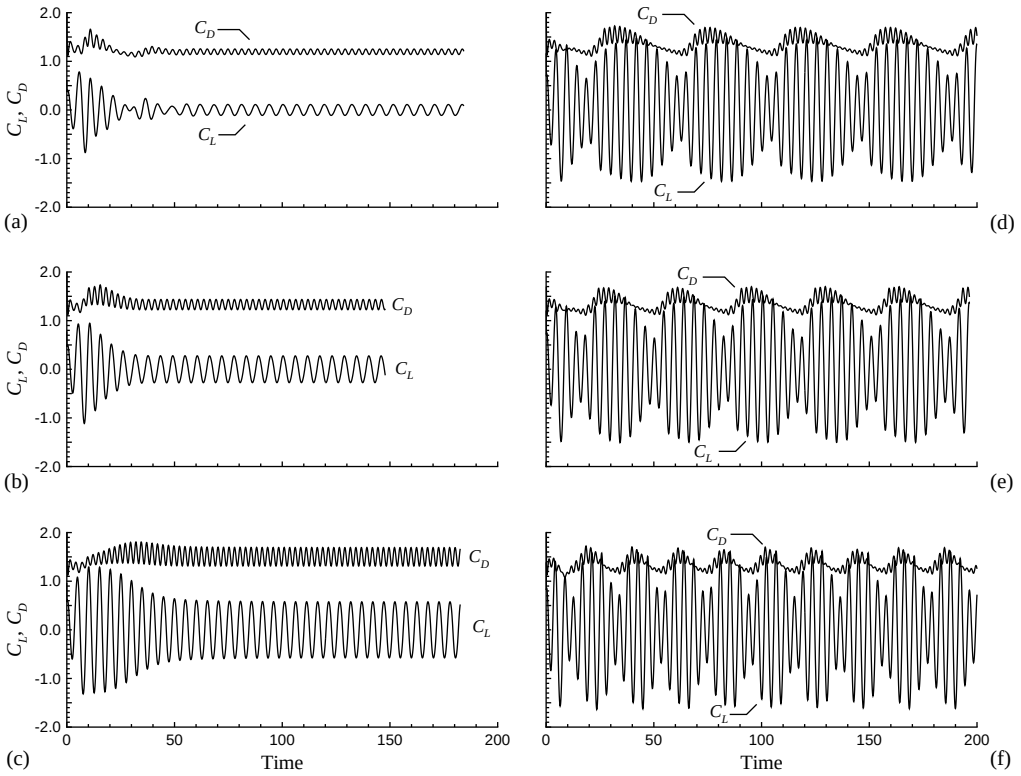

Figure 10. Drag and lift coefficients versus time for Re = 185 and $A_e/D = 0{\cdot}2$ for values of f_e/f_o equal to: (a) 0·80; (b) 0·90; (c) 1·00; (d) 1·10, (e) 1·12; (f) 1·20.

Figure 11 shows the instantaneous streamlines when the oscillating cylinder is at the extreme upper position for the same set of parameters as those in Figure 10. For values of f_e/f_o between 0·8 and 1·0, the general form of the streamline topology is the same. At $f_e/f_o = 1{\cdot}1$, Figure 11d, the pattern exhibits a radical change; it shows two saddle points in the form of intersecting streamlines. This basic description persists up to the highest value of excitation frequency. Furthermore, the centres of the closed streamlines suggest the existence of vorticity concentrations in those regions.

Corresponding contours of constant vorticity are given in the overview of Figure 12. The length of the elongated vortex attached to the upper side of the cylinder decreases as f_e/f_o increases to 1·0. As the cylinder moves up, there is vorticity formed on the cylinder base. This opposite-sign base vorticity interacts with the vorticity in the upper shear layer to diminish the vorticity available for roll-up in the wake. For f_e/f_o of 1·10 and more, the upper vortex has been diminished in strength to the extent that the lower vortex has become the dominant vortex and the upper vortex has rolled up tightly behind the cylinder. As f_e increases, the oscillatory velocity increases and the amount of negative base vorticity generated (Figure 13) is increased, contributing to diminish the strength and length of the upper vortex. We see a vorticity production for values of θ, the angle measured clockwise from the stagnation point, in the range 150–250° after the switch in timing of the initially formed vortex.

In order to have an estimate of the change in formation length due to cylinder oscillation, we present in Figure 14 the values of $u_{1\mathrm{r.m.s}}/U_\infty$ along the centreline of the

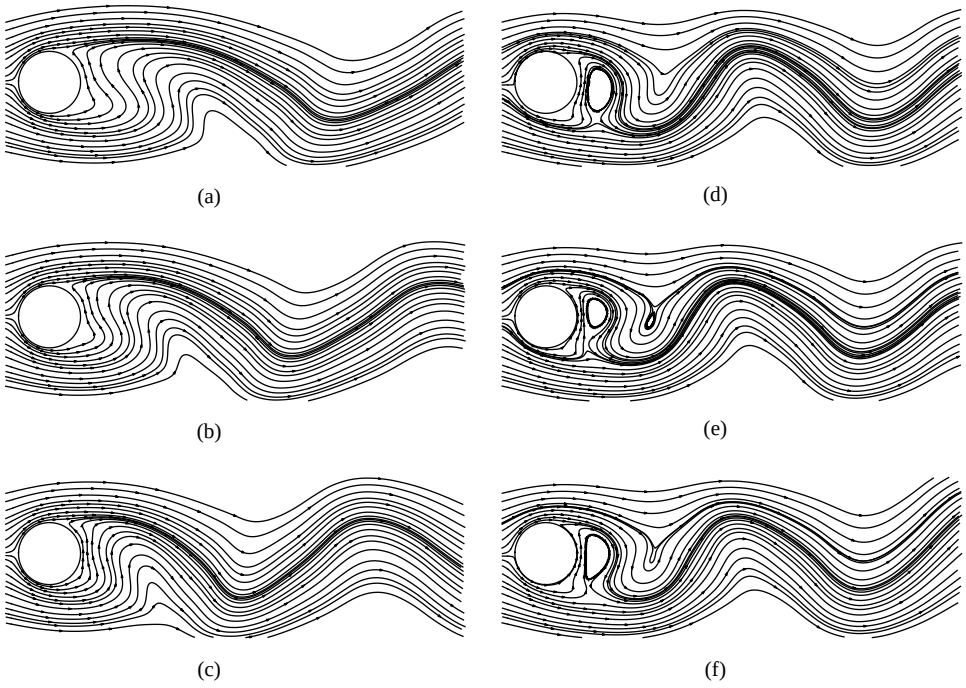

Figure 11. Instantaneous streamlines for Re = 185 and $A_e/D = 0{\cdot}2$. In all frames, the location of the cylinder is at its extreme upper position. for values of f_e/f_o equal to: (a) 0·80; (b) 0·90; (c) 1·00; (d) 1·10, (e) 1·12; (f) 1·20.

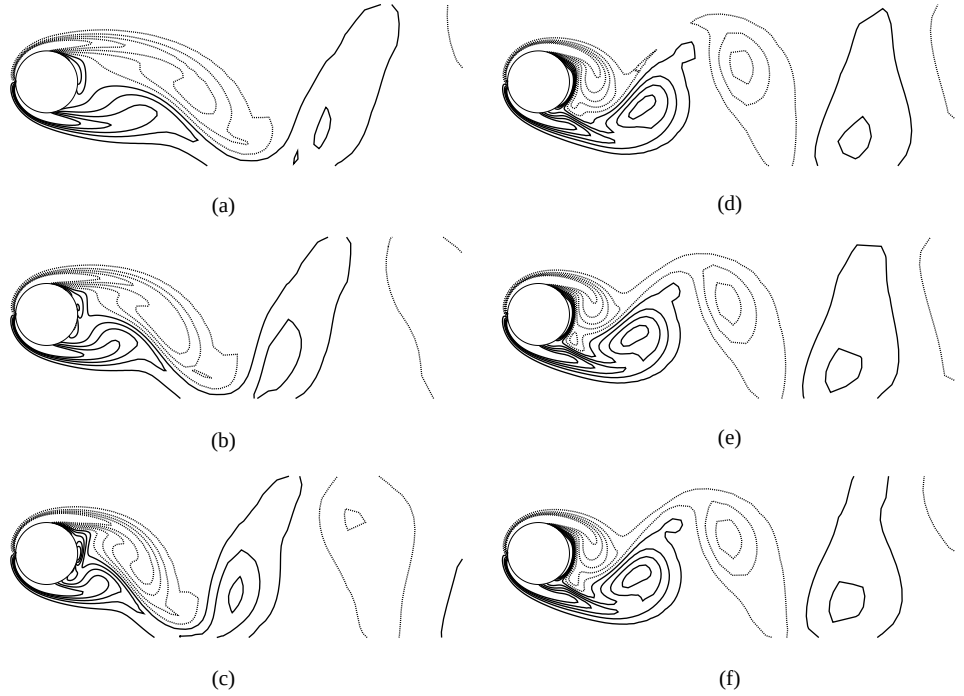

Figure 12. Instantaneous vorticity contours for Re = 185 and $A_e/D = 0{\cdot}2$. In all frames, the location of the cylinder is at its extreme upper position. for values of f_e/f_o equal to: (a) 0·80; (b) 0·90; (c) 1·00; (d) 1·10, (e) 1·12; (f) 1·20.

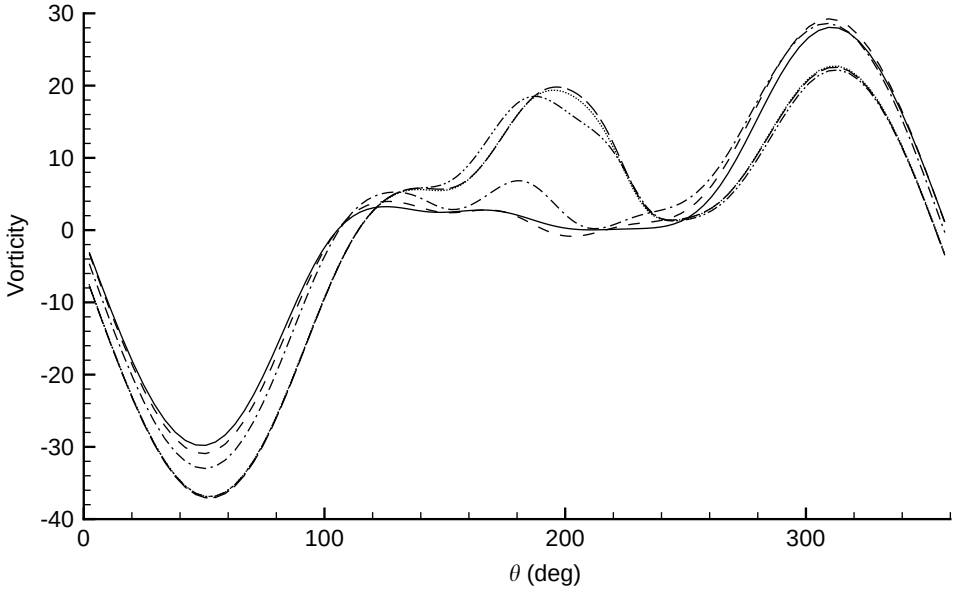

Figure 13. Vorticity at the surface of the cylinder for the range of values of f_e/f_o considered for Re = 185 and $A_e/D = 0{\cdot}2$: ————, $f_e/f_o = 0{\cdot}80$; – – – – –, $f_e/f_o = 0{\cdot}90$; – - – - – - – - –, $f_e/f_o = 1{\cdot}00$; ....., $f_e/f_o = 1{\cdot}10$; — — — — —, $f_e/f_o = 1{\cdot}12$; – - – - – - – - – - – - –, $f_e/f_o = 1{\cdot}20$; θ is the angle measured clockwise from the stagnation point. The location of the cylinder is at its extreme upper position.

wake. The formation length is estimated as being the x_1 position where the maximum $u_{1\text{r.m.s}}$ value at the centreline is reported. When the frequency of oscillation increases, the formation length decreases until a minimum length, about $0{\cdot}8D$, for a frequency of oscillation of $1{\cdot}1f_o$. If the frequency increases above this value, the formation length does not change.

A direct comparison of the streamline topologies and the distributions of vorticity is given in Figure 15 for two representative values of f_e/f_o. At $f_e/f_o = 1{\cdot}00$, it is evident that the simultaneous existence of positive (thick lines) and negative (thin lines) concentrations of vorticity in the near-wake distorts the streamline pattern without producing roll-up of the pattern. At $f_e/f_o = 1{\cdot}12$, the centre of the concentric streamline pattern behind the cylinder is approximately coincident with the concentration of vorticity.

An overlay of the contours of constant vorticity prior to, and after, the switch in timing of the initially formed vortex is given in Figure 16. All vorticity contours corresponding to the lower excitation frequency $f_e/f_o = 1{\cdot}00$ are represented by thick lines and those at $f_e/f_o = 1{\cdot}12$ by thin lines. It is evident that the pattern of the predominant concentrations of vorticity closest to the cylinder at $f_e/f_o = 1{\cdot}12$ is approximately a mirror image of that at the lower frequency $f_e/f_o = 1{\cdot}00$.

The pressure coefficient distributions are shown in Figure 17 when the location of the cylinder is at its maximum positive position. When the switch of sides of the larger vortex occurs, the pressure coefficient becomes more negative for $\theta \sim 90^\circ$. This minimum value drops sharply as f_e/f_o goes from 1·0 to 1·1.

Information about the force coefficients, in the inertial reference frame, at Re = 185 and $A_e/D = 0{\cdot}2$ is presented in Figure 18(a). The phase angle between the lift coefficient and the vertical displacement of the cylinder is presented in Figure 18(b). The time-averaged drag coefficient is seen to peak at $f_e/f_o = 1{\cdot}0$, as expected, and then decreases as f_e/f_o

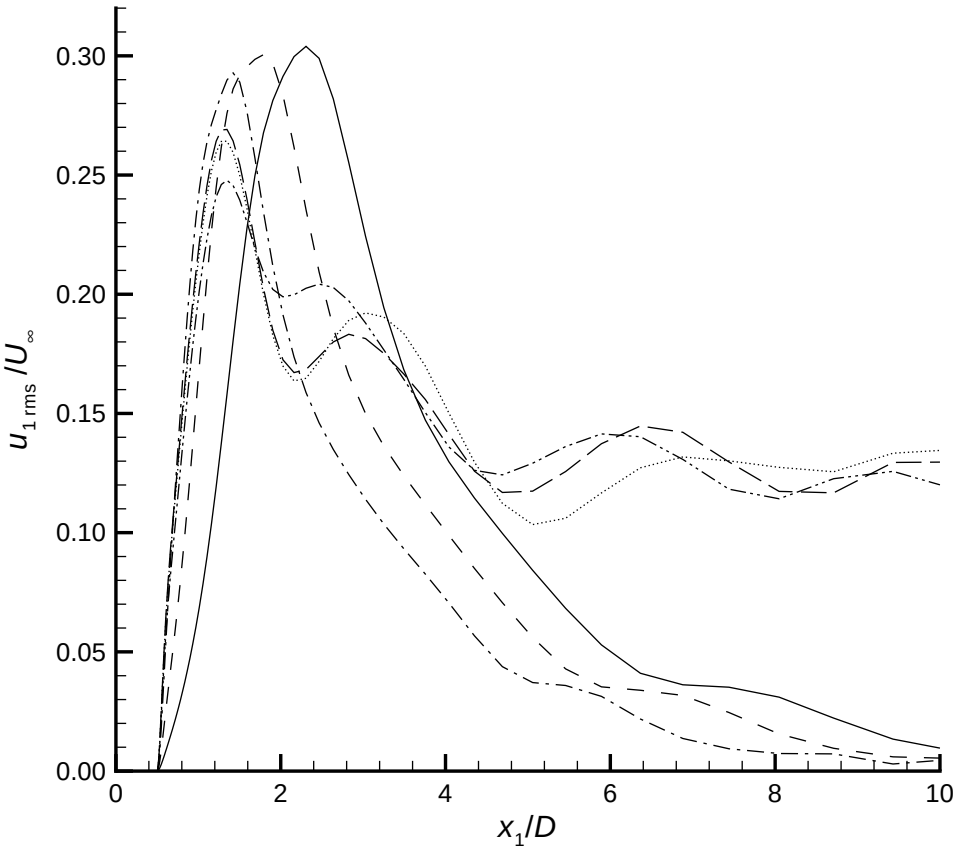

Figure 14. Values of $u_{1\mathrm{r.m.s}}/U_\infty$ along the centerline of the wake for different frequencies of oscillation, Re = 185 and $A_e/D = 0{\cdot}2$: ————, $f_e/f_o = 0{\cdot}80$; – – – – –, $f_e/f_o = 0{\cdot}90$; – – – – – – – – –, $f_e/f_o = 1{\cdot}00$; ....., $f_e/f_o = 1{\cdot}10$; — — — — —, $f_e/f_o = 1{\cdot}12$; – – – – – – – – – –, $f_e/f_o = 1{\cdot}20$.

increases. The r.m.s value of the lift coefficient and the phase angle ϕ present a change at $f_e/f_o = 1{\cdot}10$ when the vortex switching occurs.

The instantaneous streamlines are in good agreement with the experimental patterns. In Figure 11, we note that the prediction of the vortex switching produces at f_e/f_o in the range 1·00–1·10, whereas experimentally, this switching produces at f_e/f_o in the range 1·10–1·12. Figure 19 shows a comparison of streamline patterns between our numerical prediction at $f_e/f_o = 1{\cdot}10$ at which vortex switching exists and the experimental results which produces this phenomenon at $f_e/f_o = 1{\cdot}12$. At the excitation frequency $f_e/f_o = 1{\cdot}1$, we simulate the flow with different grid sizes and the same time step. The time average and the r.m.s values of drag coefficient, the r.m.s value of lift coefficient, the Strouhal number, St and the phase angle are reported in Table 3. With the coarse grid, the phenomenon of vortex switching does not appear; the phase angle between the lift coefficient and the cylinder displacement is higher than the value obtained with the refined meshes. The Strouhal number is given for information purpose and is the same with all grids. It is independent of the flow pattern. Then, this parameter is not a criterion to verify the grid convergence. With the 120×100 grid, we have a difference lower than 4% for the drag coefficient and a difference lower than 2% for the lift coefficient when compared to the value obtained with the

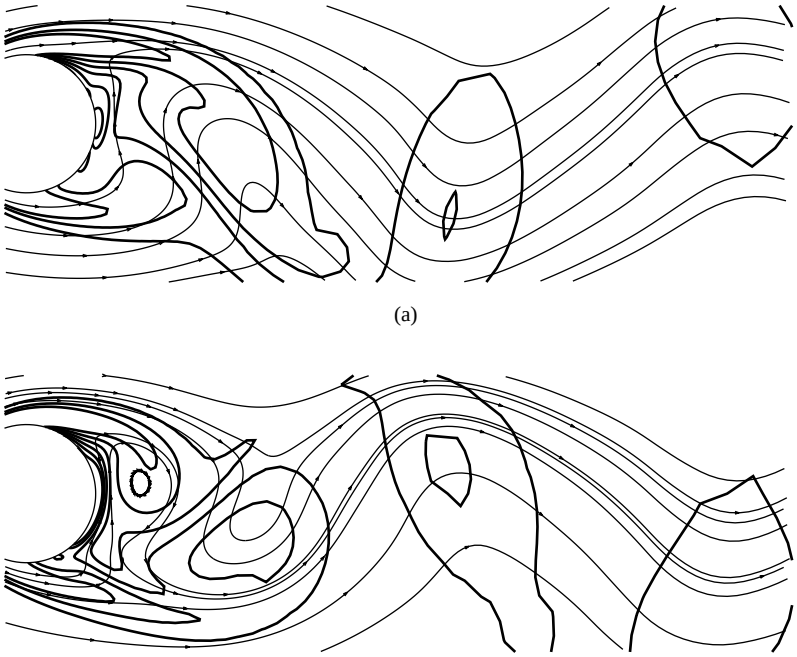

(a)

(b)

Figure 15. Superposition of instantaneous streamlines (thin lines) and contours of constant vorticity (thick lines) for Re = 185 and $A_e/D = 0{\cdot}2$ (upper position of the oscillating cylinder). (a) $f_e/f_o = 1{\cdot}00$; (b) $f_e/f_o = 1{\cdot}12$.

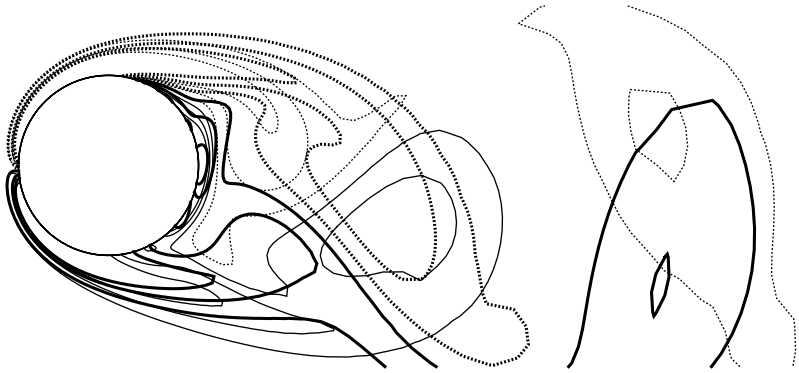

Figure 16. Superposition of the contours of constant vorticity at values of frequency ratio $f_e/f_o = 1{\cdot}00$ (thick lines) and 1·12 (thin lines) for Re = 185 and $A_e/D = 0{\cdot}2$ (——: positive values; - - - : negative values). The location of the cylinder is at its extreme upper position.

240×200 grid. Then, following this grid sensitivity study, we estimate that the resolution needed to capture an accurate solution has been obtained.

5. CONCLUSIONS

The present paper summarizes numerical results of viscous flow around an oscillating cylinder. Two configurations are investigated: cross-flow oscillations and in-line oscillations.

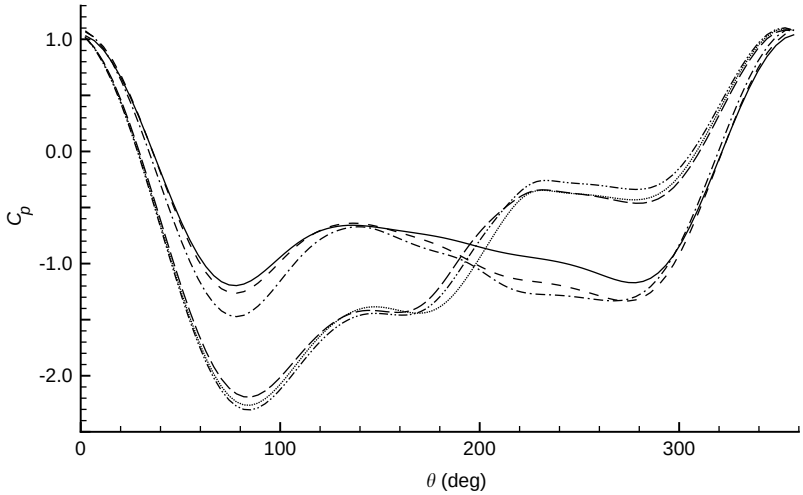

Figure 17. Pressure coefficient at the surface of the cylinder for the range of values of f_e/f_o considered for Re = 185 and $A_e/D = 0{\cdot}2$: ————, $f_e/f_o = 0{\cdot}80$; – – – – –, $f_e/f_o = 0{\cdot}90$; – - – - – - – - –, $f_e/f_o = 1{\cdot}00$; ....., $f_e/f_o = 1{\cdot}10$; — — — — —, $f_e/f_o = 1{\cdot}12$; – - – - – - – - –, $f_e/f_o = 1{\cdot}20$; θ is the angle measured clockwise from the stagnation point. The location of the cylinder is at its extreme upper position.

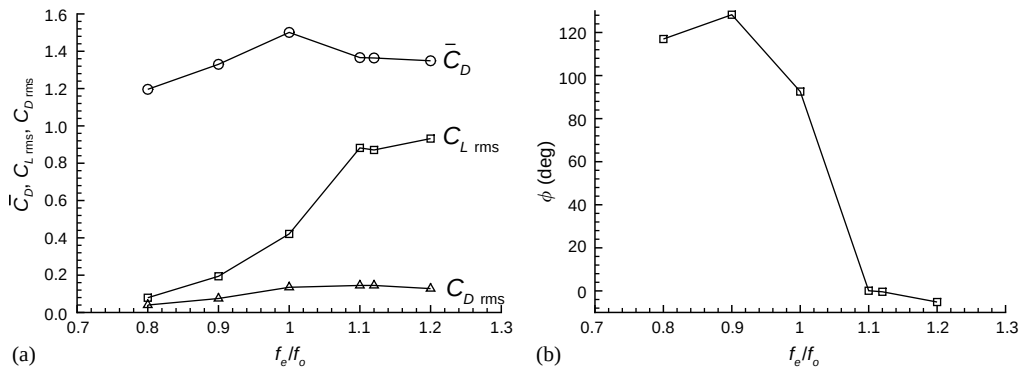

Figure 18. Force coefficients and phase angle for Re = 185 and $A_e/D = 0{\cdot}2$. (a) Time-averaged values of C_D, $\bar{C}_R$, and r.m.s. values of C_D and C_L; (b) phase angle between C_L and X_2.

The first study investigates the flow induced by harmonic oscillations of a cylinder in a fluid at rest. This case is characterized by the Reynolds number, Re = 100, and the Keulegan–Carpenter, KC = 5. With these parameters, a periodic vortex formation results, consisting of vortices with symmetrical locations with respect to the line of motion of the oscillating cylinder. Good agreement is obtained between experimental results and corresponding numerical flow predictions.

For the second study, we examine the mechanisms of vortex switching from one side of the cylinder to the other, i.e., the development of a high degree of concentration of vorticity in the wake near to the cylinder. This concentration of vorticity involves the entire near wake and results in a tighter vortex structure as the f_e/f_o ratio increases. This case is characterized by the Reynolds number Re = 185 , the oscillating amplitude

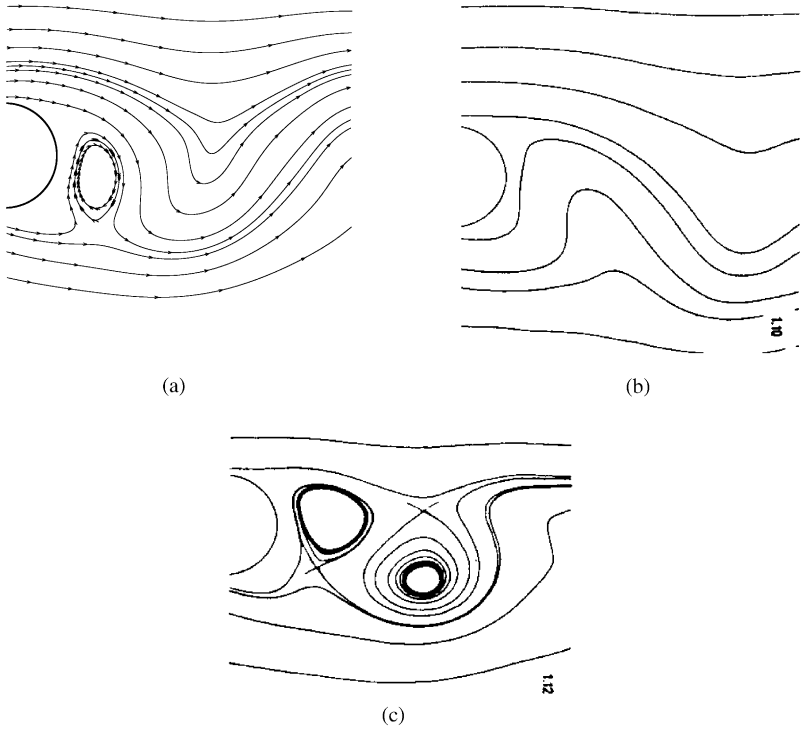

Figure 19. Comparison of streamline patterns at Re = 185 and $A_e/D = 0{\cdot}2$ (a) present computation, $f_e/f_o = 1{\cdot}10$; (b) experimental investigation (Gu *et al.* 1994), $f_e/f_o = 1{\cdot}10$; (c) experimental investigation (Gu *et al.* 1994), $f_e/f_o = 1{\cdot}12$. The location of the cylinder is at its extreme upper position

TABLE 3

Force, Strouhal number and phase angle between lift and displacement. Comparison of different grid resolutions for Re = 185, $A_e/D = 0{\cdot}2$ and $f_e/f_o = 1{\cdot}10$

	$\bar{C}_D$	$C_{D\,\text{r.m.s.}}$	$C_{L\,\text{r.m.s.}}$	St	$\phi[^\circ]$
Mesh = 120 × 50	1·595	0·163	0·574	0·214	57·86
Mesh = 120 × 100	1·366	0·145	0·882	0·214	0·07
Mesh = 120 × 200	1·351	0·136	0·881	0·214	−1·12
Mesh = 180 × 100	1·401	0·149	0·901	0·214	−0·95
Mesh = 180 × 200	1·404	0·153	0·893	0·214	−0·47
Mesh = 240 × 100	1·396	0·144	0·893	0·214	0·60
Mesh = 240 × 200	1·420	0·149	0·897	0·214	0·67

$A_e/D = 0{\cdot}2$ and the excitation frequency $0{\cdot}8 \leqslant f_e/f_o \leqslant 1{\cdot}2$. Our calculations predict that vortex switching occurs slightly earlier than the experimental data.

ACKNOWLEDGMENTS

The authors gratefully acknowledge the Scientific Committee of IDRIS (projects 98·0129 and 00·0129) for the attribution of CPU time on the Cray 98 of IDRIS. The authors are

also grateful to Stefan Becker of the Institute of Fluid Mechanics at the University of Erlangen–Nüremberg for placing the experimental data sets at our disposal.

References

Anagnostopoulos, P. 1997 Computer-aided flow visualisation and vorticity balance in the laminar wake of a circular cylinder. *Journal of Fluids and Structures* **11,** 33–72.

Bearman, P. W. 1984 Vortex shedding from oscillating bluff bodies. *Annual Reviews of Fluid Mechanics* **16,** 195–222.

Bearman, P. W. & Currie, I. G. 1979 Pressure-fluctuation measurements on an oscillating circular cylinder. *Journal of Fluid Mechanics* **91,** 661–677.

Bearman, P. W., Downie, M. J., Graham, J. M. R. & Obasaju, E. D. 1985 Forces on cylinders in viscous oscillatory flow at low Keulegan–Carpenter numbers. *Journal of Fluid Mechanics* **154,** 337–356.

Bishop, R. E. D. & Hassan, A. Y. 1964 The lift and drag forces on a circular cylinder oscillating in a flowing fluid. In *Proceedings of the Royal Society (London)*, A**277,** 51–75.

Blackburn, H. M. & Henderson, R. D. 1999 A study of two-dimensional flow past an oscillating cylinder. *Journal of Fluid Mechanics* **385,** 255–286.

Braza, M., Chassaing, P. & Minh, H. Ha 1986 Numerical study and physical analysis of the pressure and velocity fields in the near wake of a circular cylinder. *Journal of Fluid Mechanics* **165,** 79–130.

Chakrabarti, S. K. 1987 *Hydrodynamics of Offshore Structures*. Computational Mechanics Publications.

Deng, G. B., Piquet, J., Queutey, P. & Visonneau, M. 1994a Incompressible flow calculations with a consistent physical interpolation finite-volume approach. *Computers and Fluids* **23,** 1029–1047.

Deng, G. B., Piquet, J., Queutey, P. & Visonneau, M. 1994b A new fully-coupled solution of the Navier–Stokes equations. *International Journal for Numerical Methods in Fluids* **19,** 605–640.

Dütsch, H., Durst, F., Becker, S. & Lienhart, H. 1998 Low-Reynolds-number flow around an oscillating circular cylinder at low Keulegan–Carpenter numbers. *Journal of Fluid Mechanics* **360,** 249–271.

Griffin, O. M. 1971 The unsteady wake of an oscillating cylinder at low Reynolds number. *Journal of Applied Mechanics* **38,** 729–738.

Gu, W., Chyu, C. & Rockwell, D. 1994 Timing of vortex formation from an oscillating cylinder. *Physics of Fluids* **6,** 3677–3682.

Guilmineau, E., Piquet, J. & Queutey, P. 1997a Two-dimensional turbulent viscous flow simulation past airfoils at fixed incidence. *Computers and Fluids* **26,** 135–162.

Guilmineau, E., Piquet, J. & Queutey, P. 1997b Unsteady two-dimensional turbulent viscous flow past aerofoils. *International Journal for Numerical Methods in Fluids* **25,** 315–366.

Guilmineau, E., Piquet, J. & Queutey, P. 1999 A numerical study of dynamic stall on several airfoil sections. *AIAA Journal* **37,** 128–130.

Honji, H. 1981 Streaked flow around an oscillating circular cylinder. *Journal of Fluid Mechanics* **107,** 509–520.

Issa, R. I. 1985 Solution of the implicitly discretized fluid flow equations by operator-splitting. *Journal of Computational Physics* **62,** 40–65.

Justesen, P. 1991 A numerical study of oscillating flow around a circular cylinder. *Journal of Fluid Mechanics* **222,** 157–196.

Koopmann, G. H. 1967 The vortex wakes of vibrating cylinders at low Reynolds numbers. *Journal of Fluid Mechanics* **28,** 501–512.

Lin, X. W., Bearman, P. W. & Graham, J. M. R. 1996 A numerical study of oscillatory flow about a circular cylinder for low values of the beta parameter. *Journal of Fluids and Structures* **10,** 501–526.

Lu, X.-Y. & Dalton, C. 1996 Calculation of the timing of vortex formation from an oscillating cylinder. *Journal of Fluids and Structures* **10,** 527–541.

Lu, X.-Y., Dalton, C. & Zhang, J. 1997 Application of large eddy simulation to flow past a circular cylinder. *ASME Journal of Offshore Mechanics and Arctic Engineering* **119,** 219–225.

Meneghini, J. R. & Bearman, P. W. 1995 Numerical simulation of high amplitude oscillatory flow about a circular cylinder. *Journal of Fluids and Structures* **9,** 435–455.

Obasaju, E. D., Bearman, P. W. & Graham, J. M. R. 1988 A study of forces, circulation and vortex patterns around a circular cylinder in oscillating flow. *Journal of Fluid Mechanics* **196,** 467–494.

Öngoren, A. & Rockwell, D. 1988 Flow structure from oscillating cylinder, Part 1. Mechanisms of phase shift and recovery in the near wake. *Journal of Fluid Mechanics* **191,** 197–223.

Rhie, C. M. & Chow, W. L. 1983 A numerical study of the turbulent flow past an isolated aerofoil with trailing edge separation. *AIAA Journal* **17,** 1525–1532.

Sarpkaya, T. 1979 Vortex-induced oscillations—A selective review. *Journal of Applied Mechanics* **46,** 241–258.

Sarpkaya, T. 1986 Forces on a circular cylinder in viscous oscillatory flow at low Keulegan–Carpenter numbers. *Journal of Fluid Mechanics* **165,** 61–71.

Sarpkaya, T. & Isaacson, M. 1981 *Mechanics of Wave Forces on Offshore Structures*. New York: Van Nostrand Reinhold.

Schneider, G. E. & Raw, M. J. 1987 Control volume finite-element method for heat transfer and fluid flow using collocated variables. 1. Computational procedure. *Numerical Heat Transfer* **11,** 363–390.

Stansby, P. K. & Smith, P. A. 1991 Viscous forces on a circular cylinder in orbital flow at low Keulegan–Carpenter numbers. *Journal of Fluid Mechanics* **229,** 159–171.

Sun, X. & Dalton, C. 1996 Application of the LES method to the oscillating flow past a circular cylinder. *Journal of Fluids and Structures* **10,** 851–872.

Williamson, C. H. K. 1985 Sinusoidal flow relative to circular cylinders. *Journal of Fluid Mechanics* **155,** 141–174.

Williamson, C. H. K. 1988 Defining a universal and continuous Strouhal–Reynolds number relationship for the laminar vortex shedding of a circular cylinder. *Physics of Fluids* **31,** 2742–2744.

Williamson, C. H. K. 1989 Oblique and parallel models of vortex shedding in the wake of a circular cylinder at low Reynolds numbers. *Journal of Fluid Mechanics* **206,** 579–627.

Williamson, C. H. K. & Roshko, A. 1988 Vortex formation in the wake of an oscillating cylinder. *Journal of Fluids and Structures* **2,** 355–381.

Zdravkovich, M. M. 1982 Modification of vortex shedding in the synchronization range. *Journal of Applied Mechanics* **104,** 513–517.

Zhou, C. Y., So, R. M. C. & Lam, K. 1999 Vortex-induced vibrations of an elastic circular cylinder. *Journal of Fluids and Structures* **13,** 165–189.